










# Neutral cobalt(II)-bis(benzimidazole)pyridine field-induced single-ion magnets for surface deposition†

Jana Juráková, <sup>a</sup> Ondřej F. Fellner, <sup>b</sup> Sören Schlittenhardt, <sup>c</sup>  
Šárka Vavrečková,<sup>a</sup> Ivan Nemec,<sup>a,b</sup> Radovan Herchel, <sup>b</sup> Erik Čížmár, <sup>d</sup>  
Vinicius Tadeu Santana,<sup>a</sup> Milan Orlita,<sup>e</sup> Denis Gentili, <sup>f</sup> Giampiero Ruani, <sup>f</sup>  
Massimiliano Cavallini,<sup>f</sup> Petr Neugebauer, <sup>a</sup> Mario Ruben<sup>c</sup> and Ivan Šalitros <sup>\*,g</sup>

Two novel hexacoordinated Co(II)-based single-ion magnets were prepared and characterised. Both neutral complexes feature metal-centred coordination with one terminal and one bidentate nitrate anions along with tridentate derivatives of a 2,6-bis(1*H*-benzimidazole-2-yl)pyridine ligand containing either *n*-octyl (complex **1**) or *n*-dodecyl (complex **2**) chains. The presence of long aliphatic chains ensures their solubility in low polarity and volatile solvents frequently used for lithography patterning. This enabled the preparation of microstructural layers and patterns on technologically relevant substrates by easy-to-handle and low-cost wet lithographic techniques. On the other hand, attempts at surface deposition *via* sublimation were not successful due to thermal instability. The electronic structure of complexes typically features an orbitally non-degenerate ground state well-separated from the lowest excited state, which allows one to analyse magnetic anisotropy by the spin Hamiltonian approach. Zero-field splitting parameters obtained from CASSCF-NEVPT2 calculations and from the analysis of magnetic data suggest that both compounds display positive axial *D* parameters within a range of 17–25 cm<sup>−1</sup>. Combined results from high-field electron paramagnetic resonance (X-band and HF-EPR) and Fourier-transform infrared magnetic spectroscopy (FIRMS) simulated with the spin Hamiltonian provided the axial and rhombic zero-field splitting terms *D* = +23.7 cm<sup>−1</sup> for complex **1** and *D* = +24.2 cm<sup>−1</sup> for complex **2**, together with pronounced rhombicity in the range of *E/D* ≈ 0.15–0.19 for both compounds. Dynamic magnetic investigations have revealed the field-induced slow relaxation of magnetisation, with maximal relaxation times (*τ*) of 7.6 ms for **1** and 0.8 ms for **2**. This relaxation is governed *via* a combination of several relaxation mechanisms, among which the quantum tunnelling was efficiently suppressed by the applied static magnetic field. The effective barriers of spin reversal *U*<sub>eff</sub> = 77(4) K for **1** and *U*<sub>eff</sub> = 70(2) K for **2** are consistent with the expected values calculated using the ZFS parameters.

<sup>a</sup>Central European Institute of Technology, Brno University of Technology, Purkyňova 123, 61200 Brno, Czech Republic

<sup>b</sup>Department of Inorganic Chemistry, Faculty of Science, Palacký University, 17. listopadu 12, 771 46 Olomouc, Czech Republic

<sup>c</sup>Institute of Nanotechnology (INT), Karlsruhe Institute of Technology (KIT), Hermann-von-Helmholtz-Platz 1, 76344 Eggenstein-Leopoldshafen, Germany

<sup>d</sup>Institute of Physics, Faculty of Science, P.J. Šafárik University Park Angelinum 9, 04154 Košice, Slovakia

<sup>e</sup>LNCMI-EMFL, CNRS UPR3228, Univ. Grenoble Alpes, Univ. Toulouse, Univ. Toulouse 3, INSA-T, Grenoble and Toulouse, France

<sup>f</sup>Consiglio Nazionale delle Ricerche, Istituto per lo Studio dei Materiali Nanostrutturati (CNR-ISMN), Via P. Gobetti 101, 40129 Bologna, Italy

<sup>g</sup>Department of Inorganic Chemistry, Faculty of Chemical and Food Technology, Slovak University of Technology in Bratislava, Bratislava SK-81237, Slovakia.

E-mail: ivan.salitros@stuba.sk

## Introduction

Mononuclear single-molecule magnets (SMMs), also known as single-ion magnets (SIMs), offer a wide range of potential applications, including high-density data storage, quantum computing, and spintronic devices.<sup>1</sup> Unlike materials with long-range magnetic ordering, the magnetic bistability of SMMs is solely based on molecular properties and does not depend on intermolecular interactions. While initial studies have primarily focused on lanthanide SIMs, research in the last decade has revealed that mononuclear first-row transition metal complexes also exhibit interesting SIM properties. The first observation of slow relaxation of magnetisation (SRM) in mononuclear ferrous complexes by Long *et al.*<sup>2</sup> marked the beginning of a large body of research into first-row transition

metal SIMs.<sup>3</sup> High-spin Co(II) complexes are of particular interest due to their tendency to exhibit unsuppressed orbital angular momentum, resulting in significant single-ion magnetic anisotropy.<sup>4</sup> Furthermore, the non-integer ground spin state of Co(II) ions reduces the probability of quantum tunneling of magnetisation (QTM) under the applied static field, allowing a wide variety of Co(II) SIMs with various coordination numbers and geometries to be rapidly developed.

Exploring the technological applications of SIMs is challenging due to the fact that the prepared coordination compounds are typically in the form of single crystals or bulk powders, which are unsuitable for controlled manipulation and applications. Therefore, there is growing interest in fabricating nanostructured monolayers and thin films through substrate deposition. This approach combines the magnetic bistability of deposited SIMs with the electronic and/or magnetic properties of the substrate, resulting in hybrid structures that are better suited for desired applications.<sup>5</sup> Given this potential, current efforts are also focused on preparing Co(II) SIMs that are suitable for introduction on surfaces *via* sublimation<sup>6</sup> or wet deposition.<sup>7</sup> This could enable the investigation of SRM on layered or even sub-monolayered surfaces, particularly those that do not form strong covalent or non-covalent interactions with the substrates. Despite several reports proving the successful deposition by sublimation on various surfaces such as gold,<sup>8</sup> silver<sup>9</sup> and glass,<sup>10</sup> the deposited SIM molecules often exhibit diminished SMM behaviour or modified features of SRM due to interactions with the surface. Moreover, for some molecular systems, wet lithography may be a more reasonable option for maintaining their magnetic properties, as it allows for the transfer of the molecules onto substrates directly *via* chemical crafting from a solution.<sup>11</sup>

Co(II) complexes with 2,6-bis(benzimidazole-1-yl)pyridine (bbp) tridentate ligands are a well-known family of field-induced SIMs, where their rigid and aromatic ligand skeleton favours geometries supporting higher magnetic anisotropy, thus inducing a large zero-field splitting parameter  $D$ .<sup>12,13</sup> Furthermore, the rationalised introduction of aromatic or aliphatic substituents on the ligand skeleton has a significant impact on the relaxation mechanisms, which can be realized through single or multiple relaxation channels.<sup>7,14</sup> Our recent reports were focused on the pentacoordinate Co(II)-SIMs with bbp ligands functionalised by long aliphatic chains.<sup>7,15</sup> This modification enables good solubility in non-polar and volatile solvents used for lithographical deposition. Unfortunately, the weak halogenido coordination bonds are likely to have played a role in the thermal instability observed in the reported neutral pentacoordinate Co(II)-SIMs, ultimately hindering their successful surface deposition *via* sublimation. Therefore our current efforts are focused on the search for new neutral, thermally stable and sublimable Co(II)-SIMs consisting of functionalised bbp derivatives that also allow surface deposition by wet lithography approaches.

Herein we report the synthesis, and structural, spectral, magnetic and computational investigations of two neutral hexacoordinated field-induced Co(II)-SIMs (Fig. 1): complexes **1**

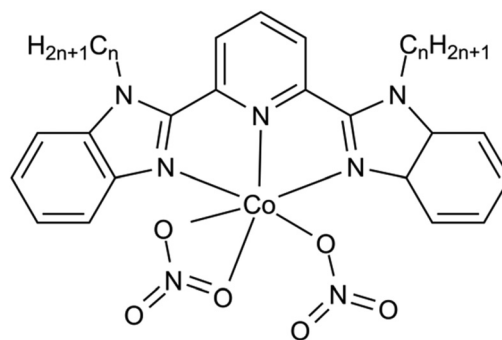


Fig. 1 Structure of reported Co(II)-SIMs **1** ( $n = 8$ ) and **2** ( $n = 12$ ).

and **2** of the general formula  $[\text{Co}(\text{L})(\text{NO}_3)_2]$ , where L corresponds to L1 = 2,6-bis(1-octyl-1H-benzimidazol-2-yl)pyridine and L2 = 2,6-bis(1-dodecyl-1H-benzimidazol-2-yl)pyridine for **1** and **2**, respectively. These complexes contain two coordinated nitrate anions, one acting as a monodentate chelating ligand and the other as a bidentate chelating ligand, and their coordination modes remain unchanged as the temperature varies. The magnetic anisotropy of the two analogues **1** and **2** was analysed by an *ab initio* theoretical approach and experimentally evaluated on the basis of static magnetic properties, X-band EPR spectroscopy and HF EPR/FIRMS spectroscopy. The alternating current (AC) susceptibility study confirmed that both complexes are field-induced SIMs and their SRM in the static magnetic field and temperature region is realised by a combination of several relaxation processes.

## Results and discussion

### Synthesis and spectral and structural properties

The detailed synthetic procedures of the hexacoordinate Co(II) complexes **1** and **2** are described in the Experimental section (see the ESI†). Their preparation is based on the reaction of  $\text{Co}(\text{NO}_3)_2 \cdot 6\text{H}_2\text{O}$  with previously reported tridentate ligands L1 and L2<sup>7</sup> in acetonitrile solution. The reactions yielded orange crystals suitable for single-crystal X-ray analysis after a few days of slow evaporation at room temperature. Their phase purity was confirmed by powder X-ray diffraction analysis before further spectroscopic and magnetic investigations were conducted (Fig. S2†). As the molecular structures of complexes **1** and **2** only differ in the length of aliphatic chains, their FT-IR (Fig. S3†) and UV-Vis (Fig. S4†) spectra are similar. The stretching vibrations of aliphatic C–H bonds were observed at intervals of 2922–2918  $\text{cm}^{-1}$  and 2854–2850  $\text{cm}^{-1}$  for asymmetric and symmetric valence vibrations, respectively. Medium vibrational bands corresponding to aromatic C–C or C–N stretching were observed in the range of 1599–1574  $\text{cm}^{-1}$ . Strong signals related to  $=\text{C}-\text{H}$  bending were found at 748  $\text{cm}^{-1}$  for both complexes. The solid-state UV-Vis absorption spectra of **1** and **2** revealed a broad band at an interval of 290–410 nm assigned to  $\pi \rightarrow \pi^*$  and  $n \rightarrow \pi^*$  transitions that split in the acetonitrile solution to  $\pi \rightarrow \pi^*$  transitions at

290 nm and to  $n \rightarrow \pi^*$  transitions at 375 nm. Furthermore, the solid-state spectra contain the second weaker band in the visible region of 500–575 nm related to d–d and MLCT transitions.

Single crystal X-ray diffraction analysis revealed that both compounds crystallise in the triclinic  $P\bar{1}$  space group at low temperatures (at 100 K for **1** and 90 K for **2**) as well as at 293 K (selected crystallographic parameters can be found in Table S1, see the ESI†). The asymmetric unit of each structure is neutral complex molecules, represented by the general formulas  $[\text{Co}(\text{L1})(\text{NO}_3)_2]$  and  $[\text{Co}(\text{L2})(\text{NO}_3)_2]$ , respectively (Fig. 2a and b). In both compounds, the Co(II) central atom is coordinated with three nitrogen atoms of the corresponding tridentate ligand and three oxygen atoms of one chelating and

one terminal nitrate anion. The structural analysis performed at two temperatures did not provide evidence for heptacoordination, which would involve the second oxygen atom of the terminal nitrate anion, as observed in similar systems previously.<sup>16</sup> At 100 K, the Co–N bond lengths of compounds vary within a tiny range of 2.088(1)–2.103(1) Å and heating to room temperature caused only small elongation to 2.100(3)–2.117(2) Å (Table S2†). Co–N bond lengths are preferably neither shorter nor longer due to coordination with the imidazole or pyridine moieties. On the other hand, Co–O coordination bonds of terminal  $\text{NO}_3^-$  anions ( $d_{\text{avg}} = 2.04$  Å for **1** and  $d_{\text{avg}} = 2.05$  Å for **2**) are notably shorter than those formed with chelating  $\text{NO}_3^-$  anions ( $d_{\text{avg}} = 2.11$  Å (O4) and 2.23 Å (O5) for **1**,  $d_{\text{avg}} = 2.10$  Å (O4) and 2.21 Å (O5) for **2**). Two oxygen donor atoms,

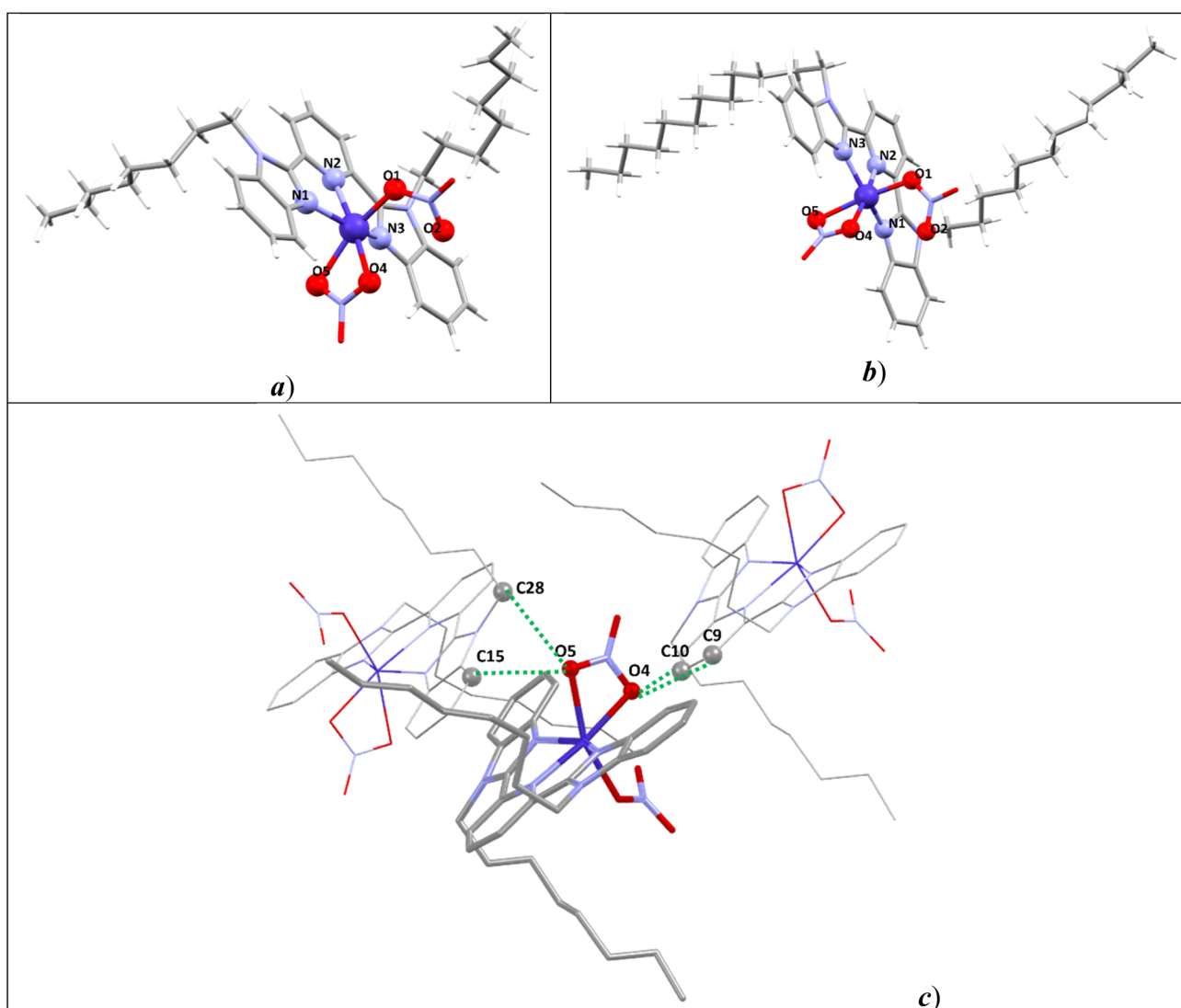


**Fig. 2** Molecular structures of **1** (a) and **2** (b). Visualisation of non-covalent interactions (green dashed lines) in compound **1** (c): O5...C15 = 3.125(2) Å, O5...C28 = 3.060(3) Å, O4...C9 = 3.183(2) Å, O4...C10 = 3.193(3) Å at 100 K; O5...C15 = 3.159(3) Å, O5...C28 = 3.195(4) Å, O4...C9 = 3.327(3) Å, and O4...C10 = 3.296(3) Å, at 293 K. Similar contacts have been found in compound **2** (Fig. S7†): O5...C5 = 3.097(2) Å, O5...C20 = 3.161(2) Å, O4...C10 = 3.132(2) Å, O4...C11 = 3.124(2) Å at 100 K; O5...C5 = 3.206(3) Å, O5...C20 = 3.210(3) Å, O4...C10 = 3.259(3) Å, and O4...C11 = 3.263(3) Å at 293 K.

O1 and O5, of the terminal and chelating NO<sub>3</sub> ligand anions, respectively, lay on the axial axis of coordination polyhedra, and their *trans* angles present the most significant contribution to the deviation from ideal octahedral geometry (avg. 159° for **1** and avg. 161° for **2**, Table S3†). The equatorial plane is formed by three N-donor atoms of the corresponding tridentate ligand and by the remaining oxygen donor atom O4 of the chelating NO<sub>3</sub> ligand anion. The symmetry measure parameters<sup>17a</sup> calculated using program SHAPE<sup>17b</sup> and the angular distortion parameter  $\Sigma$ <sup>18</sup> suggest that the coordination polyhedra of all structures can be classified as severely distorted tetragonal bipyramids ( $S(\text{OC-6})_{\text{avg}} = 5.0$ ;  $\Sigma \approx 137^\circ$ ; Table S2 and Fig. S6†). Furthermore, the second oxygen atoms O2 of terminal NO<sub>3</sub> anions create short intramolecular contacts with the Co(II) central atom with distances in the range 2.970(2)–3.013(2) Å. When those O2 oxygen atoms are hypothetically included in the coordination polyhedron, the continuous shape analysis suggests the capped octahedral ( $S(\text{COC-7})_{\text{avg}} = 5.6$ ) or capped trigonal prism ( $S(\text{CTPR-7})_{\text{avg}} = 6.3$ ) geometry.

Crystal structures of both compounds exhibit a similar motif of intermolecular interactions created by the O5 oxygen atom of chelating NO<sub>3</sub> ligand anions of one complex with phenylene C15 and alkyl C28 carbon atoms of the second neighbouring molecule. Those intermolecular synthons with distances smaller than the sum of van der Waals radii of carbon and oxygen atoms (Fig. 2c and Fig. S7†) are responsible for the formation of intermolecular pseudodimers connected to each other *via* other short contacts between the second oxygen atom O4 of the chelating NO<sub>3</sub> ligand and C9 and C10 aromatic carbon atoms of the neighbouring complex molecule.

### Surface deposition

The suitability of compounds **1** and **2** for film growth/deposition and patterning on silicon/SiO<sub>2</sub> substrates *via* wet processes was investigated using drop-casting and lithographically controlled wetting. These methods are straightforward and provide essential information for wet processing. The films and patterned structures were characterised using bright-field and polarised optical microscopes to assess the material's birefringence. Raman spectroscopy was employed to identify the compounds on the deposited surfaces, thereby confirming their stability under wet processing.

When deposited by drop-casting, chloroform solutions of **1** and **2** form continuous films that cover the entire surface, with a marked accumulation of material at the boundaries of the film generated by the so-called “coffee stain effect”.<sup>19</sup> Optical microscopy shows that the films are formed by a continuous distribution of crystals, varying in size from a few microns at the centre of the film to tens of microns at the boundaries (Fig. S8†). As expected, larger crystals (>10 µm, Fig. S8b and d†) are preferentially located at the boundaries, while micrometric crystallites are located at the centre of the sample (Fig. S8a and c†). When observed by polarised optical microscopy, the large crystals exhibit a clear birefringence. However, except in a few rare cases, the crystals extinguish the

light at precise orientation only in some portions. The crystallites in the inner areas of the film show a less intense birefringence and do not extinguish the light by rotating the polarisers in any direction. This behaviour suggests the polycrystalline nature of investigated films. Drop-casting of more diluted solutions allows for preparing surfaces with randomly distributed, irregular and droplet-like formed agglomerates, each measuring a few microns in size. These agglomerates are composed of micrometre-sized crystallites that exhibit the same behaviour as the inner part of the continuous films. Despite some minor differences in the relative peak intensity (probably due to a slightly enhanced orientation of the crystals in the printed structure compared with the powder), Raman spectra confirm that compounds **1** and **2** are processable by drop casting (Fig. S9a and c†).

Compounds **1** and **2** were also patterned on optically accessible sub-micrometric structures by lithographically controlled wetting,<sup>20</sup> a well-known wet process widely used to pattern many functional materials (see the Experimental section and ref. 21 for more details). Lithography allows large-area patterning of soluble compounds exploiting the spatial confinement provided by the formation of menisci between the protrusions of a soft stamp and the surface of the substrate.

We printed both continuous parallel stripes (obtained by the replication of a blank compact disk) and isolated sub-micrometric “pits & lands” structures equivalent to the logical pattern used in compact disks. Surfaces prepared from both compounds **1** (Fig. 3) and **2** (Fig. S10†) have similar properties and are almost indistinguishable by optical microscopy or AFM. When observed by optical microscopy, the printed structures replicate the main features of the stamp protrusions, resulting in the formation of continuous or segmented parallel stripes. Printed structures appear variously coloured and show moderate birefringence. Upon conducting a thorough investigation using polarised optical microscopy, it was observed that individual stripes did not simultaneously block light around their entire perimeter. Instead, only specific areas were found to block light, and these areas changed depending on the rotation of the polarisers. Additionally, AFM investigation of the morphology within the printed structures revealed the presence of small crystal-like substructures inside the stripes. Both polarised optical microscopy and AFM suggest that surfaces of **1** and **2** were prepared by lithographically controlled wetting from polycrystalline structures. Also here, the Raman spectra confirmed the presence of **1** and **2** on the patterned surfaces (Fig. S9b and d†).

To obtain a comprehensive understanding of the deposition capabilities of the reported Co(II) complexes, we tested the surface deposition *via* thermal sublimation of **1** and **2** onto graphene, silicon wafers and gold substrates. To facilitate deposition, we utilized an in-house built high-vacuum sublimation chamber with an outfitted quartz crucible heated with a silicon nitride heater. Additionally, a thermocouple in thermal contact with the crucible is used to achieve precise temperature control. The base pressure inside the chamber is maintained at a low level of  $1 \times 10^{-6}$  mbar. Complexes **1** and **2**

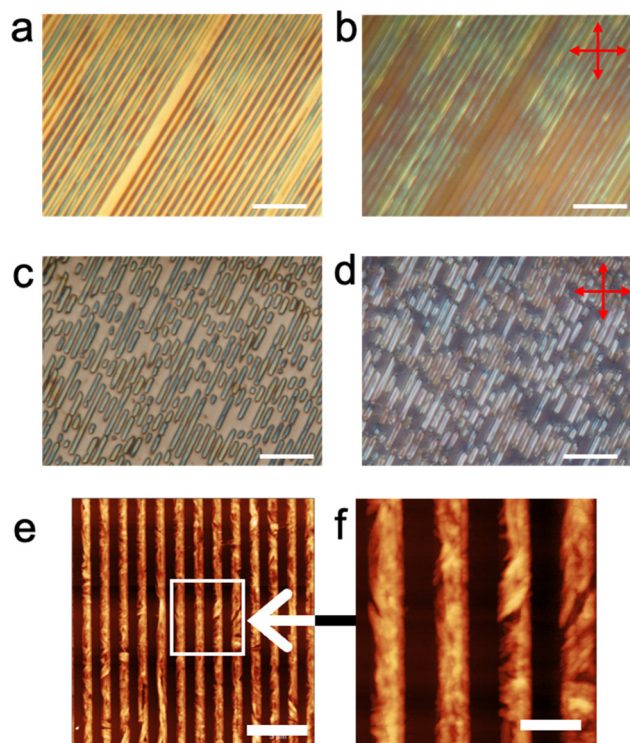


**Fig. 3** Printed structures of **1** fabricated by lithographically controlled wetting on a silicon surface: image of continuous stripes taken in bright field (a) and corresponding image under crossed polars (bar is 10  $\mu\text{m}$ ) (b). Image of microstructures taken in bright field (c) and corresponding image under crossed polars (bar is 10  $\mu\text{m}$ ) (d) AFM morphology of printed stripes (bar is 5  $\mu\text{m}$ , z scale 0–50 nm) (e); and zoomed-in (f) image of picture (e) with 1 bar = 1.5  $\mu\text{m}$ , z scale 0–45 nm.

began to sublime at temperatures of 270  $^{\circ}\text{C}$  and 310  $^{\circ}\text{C}$ , respectively, which are notably higher than their decomposition temperature (209  $^{\circ}\text{C}$  for **1**, 219  $^{\circ}\text{C}$  for **2**, Fig. S5†). This suggests that the complexes were unable to withstand the heating process and only the uncoordinated ligands were sublimed and deposited onto the selected surfaces. To determine whether the compounds remained intact after sublimation and deposition onto the surface, we employed X-ray photoelectron spectroscopy (XPS) as a surface-sensitive analytical technique. By comparing the as-synthesised bulk powder, powder after sublimation, and deposited samples, we aimed to investigate any potential degradation of the compounds. Additional information can be found in Fig. S11 and S12 in the ESI.† The absence of Co 2p and “NO<sub>3</sub>” nitrogen photoelectron peaks on the surfaces indicates that the complexes underwent partial decomposition during the sublimation and deposition process.

### Computational study and static magnetic investigation

To elucidate the connection between the magnetic anisotropy of the investigated compounds and their structural properties, we conducted a computational study with multiple objectives. First, we concentrated on the role of the nitrate ligand, which

coordinates the Co(II) atom in a monodentate manner. The second oxygen atom pointing towards the central atom adopts a rather large Co...O2 distance in both compounds (in  $\text{\AA}$ , 3.013(1) in **1** and 2.997(1) in **2** at 100 K). Nevertheless, previously, we found that even such large distances can affect the static and dynamic magnetic properties of Co(II) complexes.<sup>22</sup> Therefore, to properly analyse structures of the complex molecules in **1** and **2** we performed single-point DFT calculations at the B3LYP def-TZVP level of theory using Orca 4.2.1 computational package.<sup>23</sup> The coordinates were taken from the corresponding crystal structures as determined by X-ray diffraction, and the positions of the hydrogen atoms were optimized (B3LYP and def2-SVP).<sup>24</sup> Then, Bader's QTAIM analysis<sup>25</sup> using the Multiwfn program<sup>26</sup> was performed to investigate the topology of electron density. The (3,−1) bond critical points were found only in the case of regular metal–ligand bonds and not for the above-mentioned possibly long Co...O2 contact. Therefore, as another option, we investigated the values of non-covalent interaction index,<sup>27</sup> which can determine whether the nature of non-covalent interactions is attractive or repulsive. However, in this case the interaction between the atoms has a weak van der Waals character. Therefore, we may conclude that the second oxygen atom should not affect the Co(II) centre directly and significantly.

In the next step, we focused our attention on the analysis of magnetic anisotropy of **1** and **2** and the calculation of the ZFS parameters by the state average complete active space self-consistent field (SA-CASSCF)<sup>28</sup> with the wave function method complemented by N-electron valence second-order perturbation theory (NEVPT2).<sup>29</sup> Again, the experimentally determined molecular structures with optimised positions of hydrogen atoms were used as input coordinates. The basis set used for the calculation consisted of def2-SVP basis for hydrogen and carbon atoms, while def2-TZVP was used for the remaining atoms. The costs of calculations were decreased by the use of the def2/J and def2-TZVP/C auxiliary basis sets<sup>30</sup> together with the chain-of-spheres (RJCOSX)<sup>31</sup> approximation to exact exchange as implemented in ORCA. The active space was defined by seven electrons in five d-orbitals of Co(II) (CAS (7e,5o)), and all possible multiplets, 10 quartets and 40 doublets, were involved in the calculations. Aiming at determining the ligand field parameters, we also performed *ab initio* ligand field theory (AFLT) calculations.<sup>32</sup>

The results obtained for both complexes are very similar. The splitting of d-orbitals reflects the distorted octahedral geometry of the coordination polyhedron with the close-lying orbitals  $d_{xz}$  and  $d_{xy}$  and with  $d_{yz}$  having slightly higher energy, by ca. 1000  $\text{cm}^{-1}$  (Fig. 4 left). The remaining d-orbitals have much higher energy:  $d_{z^2}$  ( $\sim 7700 \text{ cm}^{-1}$ ),  $d_{x^2-y^2}$  ( $\sim 9000 \text{ cm}^{-1}$ ). Thus, the electronic configuration of the d-valence shell for both complexes is  $d_{xz}^2, d_{xy}^2, d_{yz}^1, d_{z^2}^1, d_{x^2-y^2}^1$ . In such a configuration, relatively small energy of the first excitation between the orbitals with the same  $|m_l|$  value ( $d_{xz} \rightarrow d_{yz}, |m_l| = \pm 1$ ) is a bit larger than the excitation involving a change of  $m_l$  by 1 ( $d_{xy} \rightarrow d_{yz}$ ). Therefore, a relatively large and positive  $D$  values can be expected for **1** and **2**.<sup>33</sup>

The SA-CASSCF/NEVPT2 calculations revealed that both complexes exhibit a similar splitting of the ligand-field terms



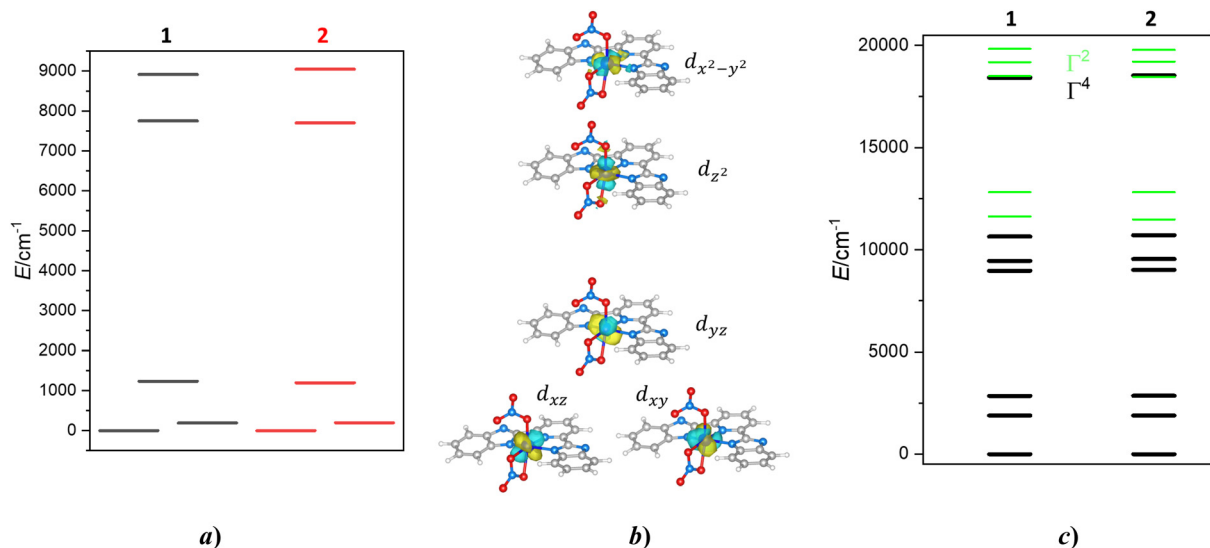


**Fig. 4** The outcome of the CASSCF/NEVPT2 calculations for complexes **1** and **2**. Plot of the d-orbital splitting calculated by *ab initio* ligand field theory (AILFT) (a), visualisations of the d-orbitals (b) and low-lying ligand-field terms (LFT) (c). Note: different multiplicities of LFT are shown in different colours.

(LFT) (Fig. 4 right). The  $^4T_{1g}$  LFT is split within the range of 0–3000  $\text{cm}^{-1}$  with the lowest excited state having energy greater than 1800  $\text{cm}^{-1}$  assuring applicability of spin Hamiltonian formalism.<sup>7,14,15</sup> The LFT's are split into ligand-field multiplets (LFM) due to spin-orbit coupling, resulting in ZFS as an energy separation between the two lowest Kramers doublets. The resulting ZFS parameters were found to be very similar for both complexes:  $D = +25.6$  (**1**) and  $+25.4$   $\text{cm}^{-1}$  (**2**) and  $E/D = 0.146$  (**1**),  $0.138$  (**2**). The effective spin Hamiltonian  $g$ -tensors calculated for **1** and **2** were practically identical, indicating easy-plane anisotropy ( $g_x \approx g_y \gg g_z$ ). This type of anisotropy in **1** and **2** was also deduced from the analysis of the first Kramers doublet using an effective spin  $S_{\text{eff}} = 1/2$ . The resulting effective  $g$ -factors are consistent with the easy-plane anisotropy ( $g_x \ll g_y \ll g_z$ ). The calculated parameters have been summarised in Table 1.

The theoretical calculations have confirmed the validity of employing the spin Hamiltonian formalism for  $S = 3/2$  in the subsequent analysis, as presented below:

$$\hat{H} = D(\hat{S}_z^2 - \hat{S}^2/3) + E(\hat{S}_x^2 - \hat{S}_y^2) + \mu_B B g \hat{S}_a \quad (1)$$

where the axial ( $D$ ) and rhombic ( $E$ ) parameters describing the zero-field splitting of quartet ground state are included

**Table 1** The theoretically calculated spin Hamiltonian parameters for complexes **1** and **2**

|          | $g_x, g_y, g_z, g_{\text{iso}}$   | $g_{x,\text{eff}}, g_{y,\text{eff}}, g_{z,\text{eff}}$<br>( $S_{\text{eff}} = 1/2$ ) <sup>a</sup> | $D/\text{cm}^{-1}$ | $E/D$ |
|----------|-----------------------------------|---------------------------------------------------------------------------------------------------|--------------------|-------|
| <b>1</b> | 2.442, 2.323, 2.097, <b>2.287</b> | 1.986, 3.592, 5.815                                                                               | +25.61             | 0.146 |
| <b>2</b> | 2.442, 2.323, 2.098, <b>2.287</b> | 2.000, 3.654, 5.766                                                                               | +25.41             | 0.138 |

<sup>a</sup> The  $g$ -parameters calculated for the ground state Kramers doublet for the effective spin  $1/2$ .

together with the Zeeman term defined for the  $a$ -direction of the magnetic field,  $B_a = B(\sin(\theta)\cos(\varphi), \sin(\theta)\sin(\varphi), \cos(\theta))$ .<sup>34</sup> Herein, we fitted both temperature and field-dependent magnetic data for **1** and **2** with the program POLYMAGNET.<sup>35</sup> Several attempts were made to analyse experimental data. Firstly, the data were fitted with the isotropic  $g$ -value and positive or negative  $D$ -parameter. Finally, the anisotropic  $g$ -tensor was also considered based on the theoretical calculations, where  $g_z$  was fixed to free electron value 2.0 and  $g_{xy}$  was allowed to vary. Here, only positive values of  $D$  were considered. The results of all three approaches are summarized in Table 2, Fig. 5 and Fig. S13, S14.† Generally, the  $|D|$  values were found in the range 15–25  $\text{cm}^{-1}$ , and it is evident that the model with anisotropic  $g$ -tensor provided higher positive values of  $D$ , which we also observed previously.<sup>36</sup> These values are also closer to those found by CASSCF/NEVPT2 calculations. Moreover, it is necessary to mention that in the case of compound **1**, the additional parameter  $\chi_{\text{TIP}}$  describing temperature-independent paramagnetism was needed to describe the steady increase of  $\mu_{\text{eff}}$  at higher temperatures. In contrast, it was revealed that the rhombic parameter  $E$  was not needed to fit magnetic data of **2** for models comprising positive  $D$ -parameter, which led to the reduction of the number of free parameters. Thus, the analysis of the static magnetic data revealed negligible differences in the magnetic anisotropy of **1** and **2**, suggesting that different relaxation properties of these compounds (*vide infra*) are not linked to their magnetic anisotropy.

## HF EPR and FIRMS spectroscopy

To corroborate the findings from the static magnetic measurements and computational studies, we utilised high-frequency electron paramagnetic resonance (HF EPR) and Fourier-trans-

**Table 2** The spin Hamiltonian parameters derived from the DC magnetic data of **1** and **2**<sup>a</sup>

| Compound | $D$ (cm <sup>-1</sup> ) | $E$ (cm <sup>-1</sup> ) | $g$ -Factors                  | $\chi_{\text{TIP}}$ (10 <sup>-9</sup> m <sup>3</sup> mol <sup>-1</sup> ) | RSS <sup>b</sup> |
|----------|-------------------------|-------------------------|-------------------------------|--------------------------------------------------------------------------|------------------|
| <b>1</b> | +19.5 (2.8)             | +6.4 (1.7)              | $g_{\text{iso}} = 2.253(18)$  | 5.8 (2.9)                                                                | 0.000272         |
|          | -20.6 (2.4)             | -5.0 (1.7)              | $g_{\text{iso}} = 2.254(18)$  | 5.7 (2.9)                                                                | 0.000296         |
|          | +24.0 (4.8)             | +7.9 (2.3)              | $g_{xy} = 2.335(24)$          | 7.3 (3.2)                                                                | 0.00100          |
|          |                         |                         | $g_z = 2.0^c$                 |                                                                          |                  |
| <b>2</b> | +17.06 (27)             | 0                       | $g_{\text{iso}} = 2.3920(22)$ | 0                                                                        | 0.000477         |
|          | -14.46 (41)             | -4.77(41)               | $g_{\text{iso}} = 2.3919(36)$ | 0                                                                        | 0.000436         |
|          | +25.71 (30)             | 0                       | $g_{xy} = 2.5264(17)$         | 0                                                                        | 0.0000198        |
|          |                         |                         | $g_z = 2.0^c$                 |                                                                          |                  |

<sup>a</sup> The standard deviation of fitted parameters are listed in parentheses. <sup>b</sup> The residual sum of squares, RSS, was calculated as  $\text{RSS} = \sum (M_{\text{calc.}} - M_{\text{exp.}})^2$ , where  $M_{\text{calc.}}$  and  $M_{\text{exp.}}$  are calculated and experimental values of molar magnetisation. <sup>c</sup> Value of  $g_z$  was fixed to 2.0.

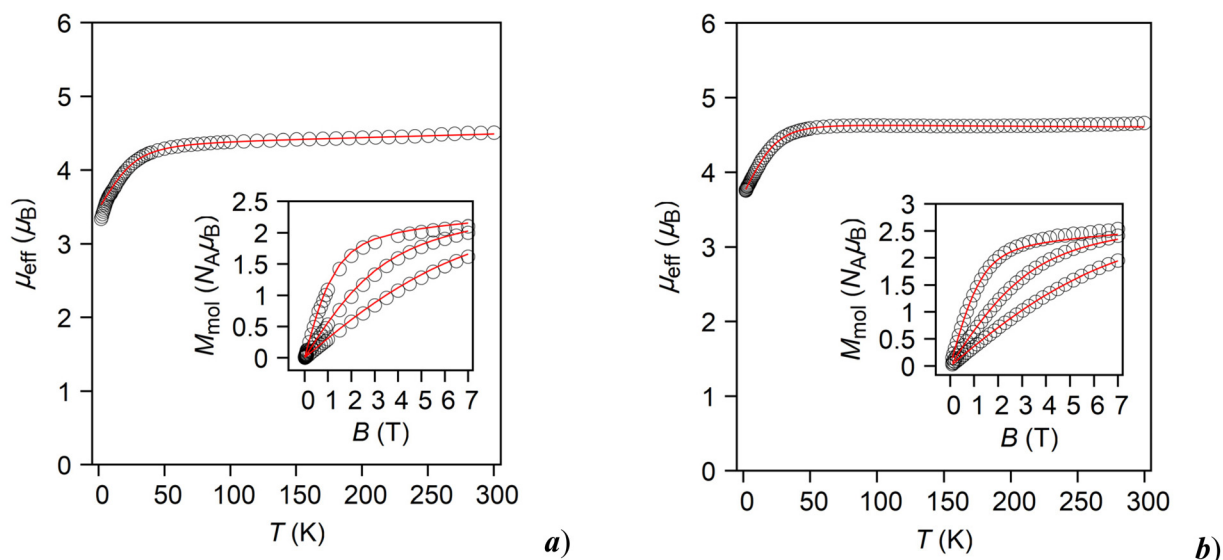


**Fig. 5** Temperature dependence of the effective magnetic moment and isothermal magnetisations measured at  $T = 2, 5$  and  $10$  K (shown in the inset) for **1** (a) and **2** (b). Empty symbols – experimental data, full lines – calculated data with  $D = +24.0$  cm<sup>-1</sup>,  $E = +7.9$  cm<sup>-1</sup>,  $g_{xy} = 2.335$ ,  $g_z = 2.000$ , and  $\chi_{\text{TIP}} = 7.3 \times 10^{-9}$  mol m<sup>-3</sup> for **1**, and  $D = +25.71$  cm<sup>-1</sup>,  $E = 0$  cm<sup>-1</sup>,  $g_{xy} = 2.5264$ , and  $g_z = 2.000$  for **2**.

form infrared magnetic spectroscopy (FIRMS) for complexes **1** and **2**. These techniques are accurate tools for determining the  $g$ -factors and ZFS in molecular magnets, especially those based on transition metals.<sup>37</sup> The results presented below can be compared in methodological aspects to several examples of quantitative ZFS determination in Co(II)-based complexes reported in the literature using a similar approach.<sup>38</sup> HFEPR spectra shown in Fig. 6 were obtained for both compounds at 5 K. Only three resonance peaks with typical effective  $g$ -factors of the Kramers doublet with  $m_s = \pm \frac{1}{2}$  were observed, suggesting a positive  $D$  in agreement with the theoretical predictions. This conclusion is further supported by the temperature dependence (shown for **1** in Fig. S15†), where the signal intensity decreases, indicating the depopulation of the ground state.<sup>38d,e</sup> Moreover, no other additional peaks for  $m_s = \pm 3/2$  are observed. FIRMS spectra shown in Fig. 7 were processed as contour plots to help visualise the clear resonance shift with the magnetic field and facilitate the fitting of the frequency

versus magnetic field dependence of the magneto-optical transmissions. Furthermore, this type of plot helps in graphically visualising the ZFS values. In Fig. S16,† the raw FIRMS data divided by the reference show a very strong feature independent of the magnetic field, possibly a phonon mode, that hinders the adequate visualization of the magnetic absorption. Therefore, we used a different type of normalization, dividing the signal at a given magnetic field by the signal from the previous magnetic field, allowing us to get rid of the peaks that do not shift with magnetic field as described in the ESI.† It is a common practice to search for the normalization that evidences the shifting features. The samples of complexes **1** and **2** were prepared in a similar way and both had a reasonable transmission intensity; however, complex **2** displayed a less intense magnetic-related peak. The reason for the intensity is not related to the concentration and there is no trivial answer to why the magnetic features behave differently in each case. This type of behavior in magnetic FTIR among similar com-

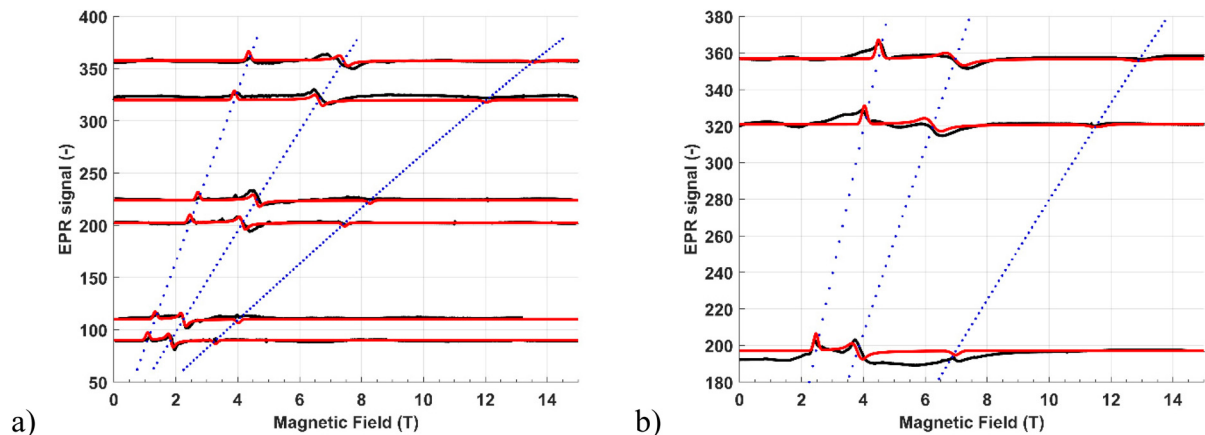


**Fig. 6** HFEPR spectra – red – using pressed powder pellets of **1** (a) and **2** (b) measured at  $T = 5.0$  K and several frequencies (y axis values correspond to the measurement frequency in GHz). Red lines are spectral simulations and blue dots are frequency-field dependence simulations using Easyspin with  $D = +23.7 \text{ cm}^{-1}$ ,  $E/D = 0.184$ ,  $g_x = 2.45$ ,  $g_y = 2.38$ , and  $g_z = 2.16$  for **1**, and  $D = +24.2 \text{ cm}^{-1}$ ,  $E/D = 0.162$ ,  $g_x = 2.48$ ,  $g_y = 2.35$ , and  $g_z = 2.19$  for **2**.

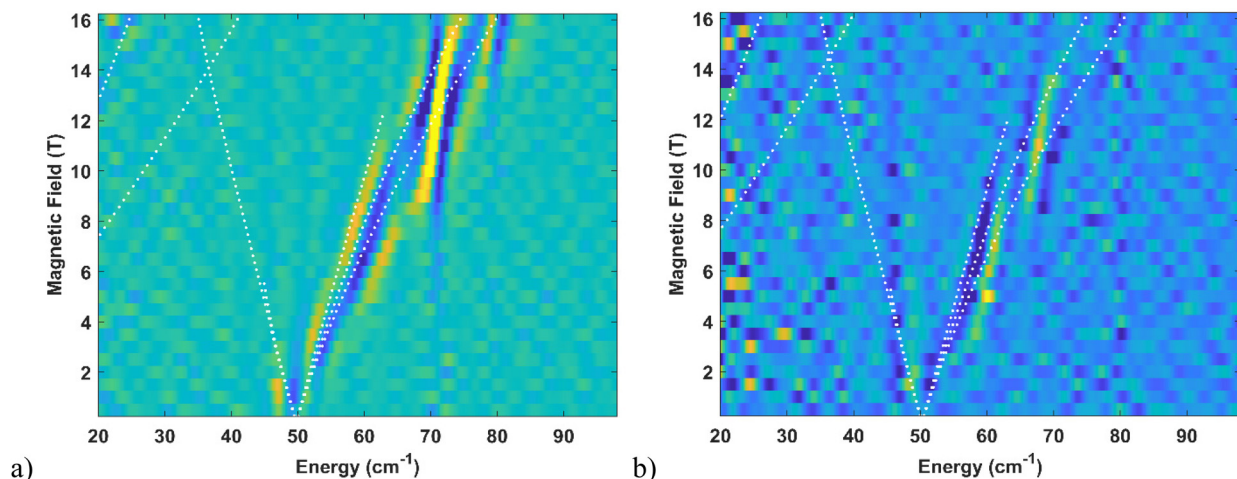


**Fig. 7** Contour plots of the derivative of the normalised FIRMS transmission spectra recorded for pressed powder pellets of **1** (a) and **2** (b) measured at  $T = 4.2$  K and a magnetic field of up to 16 T. The spectra were normalised by dividing them by the zero-field transmission spectrum, and at each magnetic field, by the spectrum from the previous magnetic field. The derivative highlights the shifts in magnetic field-dependent lines. Dots are simulation using Easyspin with  $D = +23.7 \text{ cm}^{-1}$ ,  $E/D = 0.184$ ,  $g_x = 2.45$ ,  $g_y = 2.38$ , and  $g_z = 2.16$  for **1**, and  $D = +24.2 \text{ cm}^{-1}$ ,  $E/D = 0.162$ ,  $g_x = 2.48$ ,  $g_y = 2.35$ , and  $g_z = 2.19$  for **2**.

pounds has also been observed in other materials in our previous studies.<sup>7,15</sup> Although we still do not have a satisfactory explanation yet, we are working to understand the influence of the spin-phonon coupling.<sup>39</sup> Indeed, as it will be shown in the dynamic magnetic investigation section, complex **1** has a much faster relaxation than complex **2** and this coincides with the fact that the magnetic peak has a stronger intensity in **1** compared to **2**. At this stage, there is not enough evidence to assure that this correlation implies any cause and effect. Therefore, this topic will be explored in our future works.

The results from HFEPR and FIRMS measurement techniques were analysed using the spin Hamiltonian approach for a high-spin Co(II) system with  $S = 3/2$  according to the theoretical predictions. The simulations were conducted using

Easyspin, an open-source MATLAB toolbox for simulating and fitting EPR spectra.<sup>38</sup> The parameters obtained from magnetisation and theoretical calculations were used as starting points for the fittings. The simulation of the HFEPR results was used to accurately determine the  $g$ -factors and the rhombic  $E$  values, as the available experimental frequency range was insufficient for ascertaining the axial  $D$  values. In contrast, FIRMS simulation was employed to obtain the precise ZFS as  $\Delta = 2\sqrt{D^2 + 3E^2}$ . Consequently, FIRMS simulations were conducted using the  $g$  and  $E$  values from HFEPR simulations to obtain the  $D$  values. These  $D$  values were then utilised to refine the HFEPR simulations. This iterative process was carried out for each sample until a satisfactory agreement between experimental and simulated data for both techniques was achieved.



**Table 3** Spin Hamiltonian parameters based on HFEPR and FIRMS simulation for complexes **1** and **2**

|          | $g_x, g_y, g_z, g_{iso}$ | $D/\text{cm}^{-1}$ | $E/D$ |
|----------|--------------------------|--------------------|-------|
| <b>1</b> | 2.45, 2.38, 2.16, 2.33   | +23.7              | 0.184 |
| <b>2</b> | 2.48, 2.35, 2.19, 2.34   | +24.2              | 0.162 |

The results are shown in Fig. 6 and 7 for HFEPR and FIRMS, respectively. The common parameters obtained from the simulations are shown in Table 3.

### X-band EPR investigation

The X-band EPR spectra of compounds **1** and **2** were measured in the temperature range from 2 K to 60 K displaying a decrease of the signal intensity with a substantial line broadening with increasing temperature typical of large zero-field

splitting in Co(II) complexes (Fig. S17†). In this case, it is meaningful to use a simplified effective spin  $S_{\text{eff}} = 1/2$  model describing the ground Kramers doublet for the analysis of EPR at low temperatures. This model assumes the mixing of higher excited states with the ground Kramers doublet as the consequence of the spin-orbit coupling yielding highly anisotropic effective  $g$ -factors observed in the experimental data. The simulation of EPR spectra shown in Fig. 8 was performed using the EasySpin simulation package,<sup>40</sup> including the influence of the unresolved hyperfine interaction  $A$  and an anisotropic convolutional broadening  $\Delta B$  (full-width at half-height). The obtained parameter set is summarised in Table 4. The obtained values of effective  $g$ -factors of the ground Kramers doublet can be easily interpreted within the Griffith-Figgis formalism<sup>41</sup> as typical values stemming from the orbital singlet  $^4A_{2g}$  as the ground electronic state with the axial field parameter  $\Delta_{\text{ax}} > 1500 \text{ cm}^{-1}$  (easy-plane anisotropy) and substantial rhombic  $\Delta_{\text{rh}}$

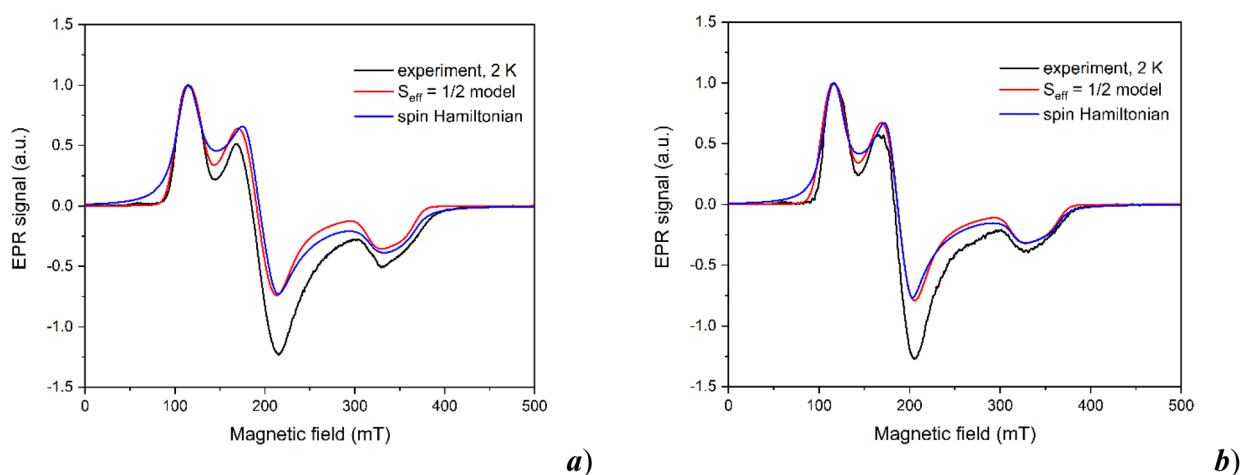


**Fig. 8** The X-band EPR data of complexes **1** (a) and **2** (b) obtained at 2 K including the simulations using the effective spin  $S_{\text{eff}} = 1/2$  model (solid red lines) and spin Hamiltonian formalism (solid blue lines) with parameters summarised in Table 3.

**Table 4** Parameters of the effective spin  $S_{\text{eff}} = 1/2$  model and spin Hamiltonian formalism estimated for the analysis of the X-band EPR for complexes **1** and **2**

| Complex, approach                                                           | Parameters                                                                                                                                         |
|-----------------------------------------------------------------------------|----------------------------------------------------------------------------------------------------------------------------------------------------|
| <b>1</b> , $S_{\text{eff}} = 1/2$ model, estimated from data                | $[g'_1, g'_2, g'_3] = [1.97, 3.47, 5.80]$ , $[A'_1, A'_2, A'_3] = [180, 200, 300]$ MHz<br>$[\Delta B_1, \Delta B_2, \Delta B_3] = [20, 50, 50]$ mT |
| <b>1</b> , $S_{\text{eff}} = 1/2$ model, $x, y, z$ assignment <sup>40</sup> | $[g'_x, g'_y, g'_z] = [3.47, 5.8, 1.97]$ , $[A'_x, A'_y, A'_z] = [200, 300, 180]$ MHz<br>$[\Delta B_x, \Delta B_y, \Delta B_z] = [50, 50, 20]$ mT  |
| <b>1</b> , spin Hamiltonian, $x, y, z$ assignment <sup>40</sup>             | $[g_x, g_y, g_z] = [2.341, 2.377, 2.136]$ , $[A_x, A_y, A_z] = [134, 74, 325]$ MHz<br>$E/D = 0.178$                                                |
| <b>1</b> , spin Hamiltonian, estimated from data                            | $[g_x, g_y, g_z] = [2.34, 2.38, 2.14]$ , $[A_x, A_y, A_z] = [130, 75, 190]$ MHz<br>$E/D = 0.173$<br>$\Delta B = 25$ mT                             |
| <b>2</b> , $S_{\text{eff}} = 1/2$ model, estimated from data                | $[g'_1, g'_2, g'_3] = [1.98, 3.56, 5.77]$ , $[A'_1, A'_2, A'_3] = [180, 200, 300]$ MHz<br>$[\Delta B_1, \Delta B_2, \Delta B_3] = [20, 50, 50]$ mT |
| <b>2</b> , $S_{\text{eff}} = 1/2$ model, $x, y, z$ assignment <sup>40</sup> | $[g'_x, g'_y, g'_z] = [3.56, 5.77, 1.98]$ , $[A'_x, A'_y, A'_z] = [140, 280, 180]$ MHz<br>$[\Delta B_x, \Delta B_y, \Delta B_z] = [50, 50, 20]$ mT |
| <b>2</b> , spin Hamiltonian, $x, y, z$ assignment <sup>40</sup>             | $[g_x, g_y, g_z] = [2.342, 2.391, 2.123]$ , $[A_x, A_y, A_z] = [92, 74, 300]$ MHz<br>$E/D = 0.154$                                                 |
| <b>2</b> , spin Hamiltonian, estimated from data                            | $[g_x, g_y, g_z] = [2.34, 2.39, 2.12]$ , $[A_x, A_y, A_z] = [100, 75, 190]$ MHz<br>$E/D = 0.154$<br>$\Delta B = 20$ mT                             |

parameter. The result is consistent with the predicted positive  $D$  parameter from SA-CASSCF/NEVPT2 calculations. Having the effective  $g$ -factor components  $g'_1$ ,  $g'_2$ , and  $g'_3$  of the ground Kramers doublet estimated for the EPR spectra, one can assign them correctly to  $g'_x$ ,  $g'_y$ , and  $g'_z$  and later to real  $g$ -factors  $g_x$ ,  $g_y$ , and  $g_z$  of spin Hamiltonian formalism using an approach outlined in ref. 42. First, all possible combinations of  $g'_1$ ,  $g'_2$ , and  $g'_3$  are used to calculate six dependencies of an average real  $g$ -factor on the  $E/D$  ratio, which are checked against the average  $g$ -factor obtained from the experimental room temperature value of the effective magnetic moment. This will eventually give a single assignment of  $x$ ,  $y$ , and  $z$  components instead of the 1, 2, and 3 components of the  $g$ -factors as well as the components of the anisotropic hyperfine interaction. At the same time, the correct value of  $E/D$  is estimated from the procedure, but the values of  $D$  and  $E$  directly cannot be estimated. It is sometimes cumbersome to obtain accurate values of the average real  $g$ -factor due to uncertainties in the subtraction of diamagnetic or temperature-independent paramagnetic susceptibility. In our case, we used the average  $g$ -values predicted from SA-CASSCF/NEVPT2 calculations in Table 1, and this approach showed an excellent consistency between calculations and analysis of EPR spectra. The results are also summarised in Table 4, yielding the  $E/D$  values 0.178 and 0.154 for **1** and **2**, respectively. It should be noted that the direct estimation of spin Hamiltonian parameters  $D$  and  $E$  from the X-band EPR is also not possible for  $\text{Co(II)}$  ions with  $D > 8 \text{ cm}^{-1}$ , only the  $E/D$  ratio can be obtained. Having the  $E/D$  ratio, real  $g$ -factors, and hyperfine interactions estimated from the aforementioned analysis, we used those values as starting parameters to simulate the experimental X-band EPR spectra using spin Hamiltonian formalism with the  $D$  parameter for simplicity fixed to  $25 \text{ cm}^{-1}$ . A very good agreement with the experimental spectra was obtained with only minor corrections of the starting parameters, yielding  $E/D$  values of 0.173 and 0.154 for **1** and **2**, respectively, as shown in Fig. 8. This result is in good agreement with the SA-CASSCF/NEVPT2, HF EPR and

FIRMS analysis, confirming slightly higher rhombic anisotropy in **1**. A slight difference in  $g$ -factors obtained from X-band EPR and HFEPR can be accounted for by the different sensitivity of the two methods to the influence of hyperfine coupling, which strongly affects the lineshape of X-band data.

### Dynamic magnetic investigation

In order to probe the SIM behaviour in reported compounds, the frequency dependence of the alternating current susceptibility was measured at various fields and temperatures (see the ESI† for a detailed experimental description of AC susceptibility measurements and data analysis). At 2 K and zero DC field, no significant out-of-phase component ( $\chi''$ ) of the AC susceptibility was observed for both complexes (Fig. S18 and S19, see the ESI†). This is a consequence of the fast relaxation of magnetisation resulting from the quantum tunnelling effect induced by hyperfine interactions with the nuclear spins. However, the applied DC field in the range of 0–0.5 T caused the suppression of the tunnelling effect, and the evolution of  $\chi''$  upon frequency change at 2 K proves the field-induced slow relaxation of magnetisation in **1** and **2**. Both compounds exhibit single-channel relaxation under a weaker DC field ( $<0.3 \text{ T}$ ), and two-channel relaxation under stronger DC fields ( $>0.3 \text{ T}$  for **1** and  $>0.2 \text{ T}$  for **2**; Tables S5 and S6†). Therefore, in-phase ( $\chi'$ ) and out-of-phase components of AC susceptibility were simultaneously fitted to extended one-set and two-set Debye models (eqn (S1)–(S4)†). The low-frequency (LF) channels appeared only above 0.3 T and were not analysed further.

The evolution of field-dependent relaxation time  $\tau$  for **1** and **2** is different (Fig. 9a). Compound **1** shows one order of magnitude longer  $\tau$  with the maximal value at 0.15 T (17.6 Hz,  $\tau_{\text{max}} = 9.1 \text{ ms}$ ), while **2** reaches the maximal value at 0.07 T (17.6 Hz,  $\tau_{\text{max}} = 0.76 \text{ ms}$ ). Given the closely similar coordination environment and values of ZFS splitting parameters in both compounds (*vide supra*), the noticeable discrepancies in the relaxation time could tentatively be attributed to the varying lengths of the aliphatic chains. It is plausible to consider that

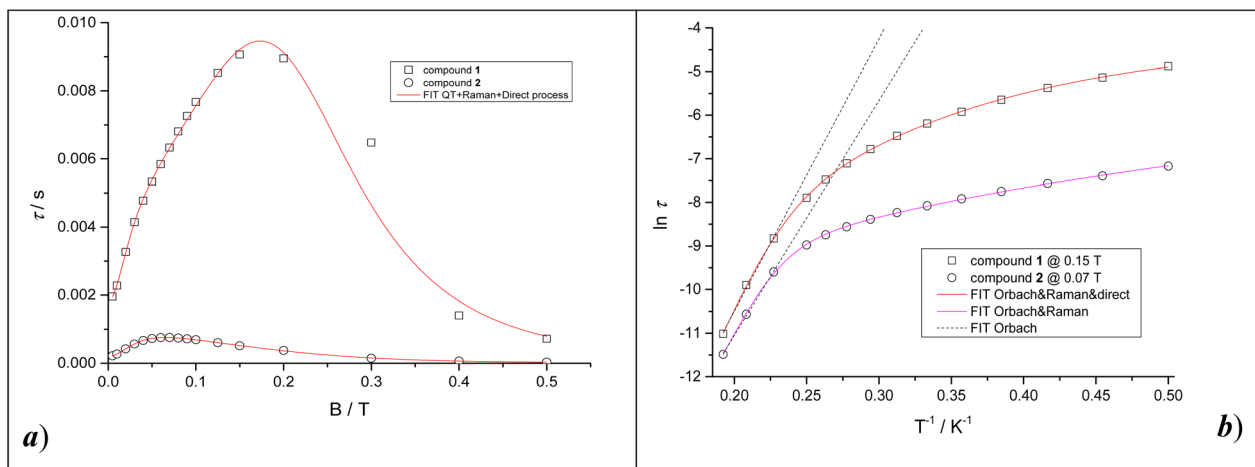


Fig. 9  $\tau$  vs.  $B$  (a) and  $\ln \tau$  vs.  $1/T$  (b) dependencies for compounds **1** and **2**.

the elongation of these chains may facilitate the interaction between the molecules and the environment through acoustic and/or optical vibrational modes, thereby influencing the relaxation dynamics. Both  $\tau$  vs.  $B$  dependencies were successfully fitted to relaxation eqn (2) which involves quantum tunnelling, direct and Raman relaxation processes.

$$\frac{1}{\tau} = \frac{b_1}{1 + b_2 B^2} + AB^m T + d \left( \frac{1 + eB^2}{1 + fB^2} \right) T^n \quad (2)$$

The fits were performed with fixed Raman and direct exponents to theoretical values  $m = 4$  and  $n = 9$ , expected for Kramer's ions.<sup>43</sup> Table S7† presents the obtained parameters  $b_1$ ,  $b_2$  (quantum tunnelling),  $A$  (direct process) and  $d$ ,  $e$ , and  $f$  (Raman process), which were used for the simulation of the individual relaxation rates and their contributions to the overall relaxation (Fig. S20†). For complex **1**, the major contribution to relaxation in the low field region is quantum tunnelling while the Raman relaxation becomes dominant with the increase of the field. Interestingly, quantum tunnelling is suppressed even at a very small field (0.005 T) for complex **2** and the Raman relaxation is the only dominant process up to ca. 0.2 T. Above 0.25 T, the major contribution to the relaxation of both compounds originates from the direct process.

The temperature-dependent dynamic studies were performed at  $B_{DC} = 0.15$  T for **1** and 0.07 T for **2**, where the slow relaxation of magnetisation lasts the longest (Fig. 9a).  $\chi''$  shows the single maxima shift from 76.3 Hz (for **1** at 1.8 K,  $\tau = 2.09$  ms) and from 331.6 Hz (for **2** at 2.0 K,  $\tau = 0.48$  ms), respectively, towards higher frequencies with the increase of the temperature (Tables S8 and S9†). The obtained frequency dependent  $\chi'$  and  $\chi''$  components of AC susceptibility were simultaneously fitted to a one-set Debye model (eqn (S1), (S2); Fig. S21, S22; and Tables S8, S9†). The obtained temperature dependencies of relaxation time  $\ln \tau$  vs.  $1/T$  were fitted with respect to relaxation eqn (3) involving the terms of direct, Raman and Orbach relaxation mechanisms, respectively

$$\frac{1}{\tau} = aTB^m + CT^n + \frac{1}{\tau_0} \exp\left(-\frac{U_{\text{eff}}}{kT}\right) \quad (3)$$

At first, the effective energy barrier of spin reversal  $U_{\text{eff}}$  was estimated by fitting the high-temperature region (4.4 K–5.2 K) to the Arrhenius-like equation of a single Orbach process, which resulted in  $U_{\text{eff}} = 62(4)$  K for **1** and  $U_{\text{eff}} = 54(2)$  K for **2** (Fig. 9b, dashed lines). The comprehensive analysis of  $\ln \tau$  vs.  $1/T$  dependencies in the whole temperature range however requires the combination of two or three relaxation mechanisms. The previous low-temperature analysis of  $\tau$  vs.  $B$  dependencies suggests that SRM in **1** is governed by Raman and direct mechanism at  $B_{DC} = 0.15$  T (Fig. S20,† solid vertical line), while for **2**, it is predominantly governed by a single Raman process at  $B_{DC} = 0.07$  T (Fig. S20,† dash-dotted vertical line). Therefore, the comprehensive fit of the  $\ln \tau$  vs.  $1/T$  dependencies was conducted using all three relaxation processes for **1**, and the combination of Orbach and Raman processes for **2**. Those two approaches resulted in relaxation parameters  $U_{\text{eff}} =$

77(4) K,  $\tau_0 = 7(2) \times 10^{-12}$  s,  $C = 0.6(1)$  K<sup>n</sup> s<sup>-1</sup>,  $n = 5.8(2)$ , and  $A = 1.00(4) \times 10^5$  s<sup>-1</sup> T<sup>4</sup> K<sup>-1</sup> for **1** and  $U_{\text{eff}} = 70(2)$  K,  $\tau_0 = 1.6(5) \times 10^{-11}$  s,  $C = 264(9)$  K<sup>n</sup> s<sup>-1</sup>, and  $n = 2.28(3)$  (Fig. 9b solid lines; Table S10†). The obtained relaxation parameters indicate that subtle structural differences between **1** and **2** cause a slight decrease of the energy barrier of spin reversal  $U_{\text{eff}}$  and accelerate the Raman relaxation. On the other hand, the relaxation governed *via* the direct process seems to be relevant only in complex **1** with a shorter *n*-octyl aliphatic chain. It is interesting to note that the values of the effective energy barriers  $U_{\text{eff}}$  are close to the theoretical ones  $U = 69$  K and  $U = 74$  K, calculated by the equation for Kramer's ions  $U = (S^2 - \frac{1}{4})|D|$  using the axial ZFS parameters obtained from the fit with anisotropic *g*-tensor (Table 2). The Raman exponents acquire smaller values than the expected value of 9 for Kramer's ions,<sup>44</sup> but when optical and acoustic phonons are considered, values in the range of 1–6 are acceptable.<sup>38</sup>

## Summary

In this paper, we report on the synthesis, crystal structure, magnetic properties and field-induced single-molecule magnetic behaviour of two structurally similar hexacoordinated Co (II) complexes with tailor-made organic ligands for wet depositions on surfaces. Both compounds have been successfully deposited onto silicon surfaces as sub-micrometric structures through drop casting and lithographically controlled wetting, mimicking the logical patterns utilized in compact disks, such as parallel stripes or isolated “pits & lands”. Although the neutral molecular structure of the complexes makes them suitable for sublimation, their thermal instability rendered this approach unsuccessful. The structural analysis unveiled the distorted octahedral shape of coordination polyhedra consisting of three nitrogen donor atoms of the corresponding tridentate ligand and three oxygen donor atoms of two nitrate anions, one of which is coordinated in a bidentate fashion and the other in a monodentate fashion. The role of the fourth oxygen atom of the monodentate nitrate ligand has been inspected in detail and it has been shown that the formed Co (II)···O noncovalent interactions do not affect the electronic structure of the central atom significantly. The comprehensive analysis of the electronic structure and magnetic properties of reported complexes **1** and **2** demonstrates their positive axial *D* parameters, easy-plane anisotropy, and applicability of the spin Hamiltonian formalism for  $S = 3/2$ . Combining *ab initio* calculations, static magnetic data, HF and X-band EPR, and FIRMS measurements, the study highlights the similarities and differences in magnetic anisotropy between the two complexes, which also influence their relaxation properties. AC susceptibility investigations demonstrated field-induced SIM behaviour in both complexes. At very low temperatures, the SRM is governed by a combination of quantum tunnelling, direct relaxation, and Raman relaxation processes. The effect of quantum tunnelling was effectively suppressed by an increased static magnetic field, which, in turn, activated relax-

ation *via* the direct mechanism. As the temperature increased, the Orbach relaxation process was also activated, with effective energy barriers that match the predicted values from the ZFS parameters.

## Author contributions

J. J.: synthesis, formal analysis, data curation, writing – original draft, and writing – review & editing; O. F. F.: formal analysis and data curation; S. S.: data curation; S. V.: data curation; I. N.: data curation, investigation, visualization, writing – original draft, and writing – review and editing; R. H.: investigation, visualization, writing – original draft, and writing – review and editing; E. Č.: data curation, investigation, visualization, writing – original draft, and writing – review & editing; V. T. S.: data curation, investigation, visualization, writing – original draft, and writing – review and editing; M. O.: data curation; D. G.: data curation and visualization; G. R.: data curation and visualization; M. C.: investigation, visualization, writing – original draft, and writing – review and editing; P. N.: conceptualization, resources, and writing – review & editing; M. R.: conceptualization, resources, and writing – review & editing; and I. Š.: conceptualization, funding acquisition, resources, supervision, data curation, writing – original draft, visualization, and writing – review & editing.

## Conflicts of interest

There are no conflicts to declare.

## Acknowledgements

Slovak grant agencies (APVV-19-0087, APVV-22-0172, DS-FR-22-0010 and VEGA 1/0029/22) are acknowledged for the financial support. J. J., I. N. V. T. S. and I. Š. acknowledge the financial support from the Grant Agency of the Czech Republic grant no. 22-23760S. This article was written with the generous support under the Operational Program Integrated Infrastructure for the project: “Strategic Research in the Field of SMART Monitoring, Treatment and Preventive Protection against Coronavirus (SARS-CoV-2)”, project no. 313011ASS8, co-financed by the European Regional Development Fund. J. J. acknowledges financial support from an internal grant from Brno University of Technology CEITEC VUT-J-22-8049. Furthermore, we acknowledge CzechNanoLab Research Infrastructure supported by MEYS CR (LM2023051). O. F. F., I. N. and R. H. acknowledge the financial support from the institutional sources of the Department of Inorganic Chemistry, Palacký University Olomouc, Czech Republic. O. F. F. acknowledges the support of MSTC Danube 8X23030 project.

## References

- 1 D. Gatteschi, R. Sessoli and J. Villain, *Molecular Nanomagnets*, Oxford University Press, Oxford, 2007.
- 2 (a) D. E. Freedman, W. H. Harman, T. D. Harris, G. J. Long, C. J. Chang and J. R. Long, Slow Magnetic Relaxation in a High-Spin Iron(II) Complex, *J. Am. Chem. Soc.*, 2010, **132**, 1224; (b) W. H. Harman, T. D. Harris, D. E. Freedman, H. Fong, A. Chang, J. D. Rinehart, A. Ozarowski, M. T. Sougrati, F. Grandjean, G. J. Long, J. R. Long and C. J. Chang, Slow Magnetic Relaxation in a Family of Trigonal Pyramidal Iron(II) Pyrrolide Complexes, *J. Am. Chem. Soc.*, 2010, **132**, 18115.
- 3 (a) A. K. Bar, C. Pichon and J.-P. Sutter, Magnetic anisotropy in two- to eight-coordinated transition-metal complexes: Recent developments in molecular magnetism, *Coord. Chem. Rev.*, 2016, **308**, 346; (b) J. M. Frost, K. L. M. Harriman and M. Murugesu, The rise of 3-d single-ion magnets in molecular magnetism: towards materials from molecules?, *Chem. Sci.*, 2016, **7**, 2470.
- 4 (a) J. Juráková and I. Šalitroš, Co(II) single-ion magnets: synthesis, structure, and magnetic properties, *Monatsh. Chem.*, 2022, **153**, 1001; (b) P. K. Sahu, R. Kharel, S. Shome, S. Goswami and S. Konar, Understanding the unceasing evolution of Co(II) based single-ion magnets, *Coord. Chem. Rev.*, 2023, **475**, 214871.
- 5 T. Blachowicz and A. Ehrmann, New Materials and Effects in Molecular Nanomagnets, *Appl. Sci.*, 2021, **11**, 7510.
- 6 J. Hruby, S. Vavreckova, L. Masaryk, A. Sojka, J. Navarro-Giraldo, M. Bartos, R. Herchel, J. Moncol, I. Nemec and P. Neugebauer, Deposition of Tetracoordinate Co(II) Complex with Chalcone Ligands on Graphene, *Molecules*, 2020, **25**, 5021.
- 7 J. Juráková, J. Dubnická-Midlíková, J. Hrubý, A. Kliuikov, V. T. Santana, J. Pavlik, J. Moncol, E. Čížmár, M. Orlita, I. Mohelský, P. Neugebauer, D. Gentili, M. Cavallini and I. Šalitroš, Pentacoordinate cobalt(II) single ion magnets with pendant alkyl chains: shall we go for chloride or bromide?, *Inorg. Chem. Front.*, 2022, **9**, 1179.
- 8 (a) E. Kiefl, M. Mannini, K. Bernot, X. Yi, A. Amato, T. Leviant, A. Magnani, T. Prokscha, A. Suter, R. Sessoli and Z. Zaher, Robust Magnetic Properties of a Sublimable Single-Molecule Magnet, *ACS Nano*, 2016, **10**, 5663; (b) L. Malavolti, V. Lanzilotto, S. Ninova, L. Poggini, I. Cimatti, B. Cortigiani, L. Margheriti, D. Chiappe, E. Otero, P. Saintavit, F. Totti, A. Cornia, M. Mannini and R. Sessoli, Nanofilament Formation and Regeneration During Cu/Al<sub>2</sub>O<sub>3</sub> Resistive Memory Switching, *Nano Lett.*, 2015, **15**, 535.
- 9 J. Hellerstedt, A. Cahlík, M. Švec, B. de la Torre, M. Moro-Lagares, T. Chutora, B. Papoušková, G. Zoppellaro, P. Mutombo, M. Ruben, R. Zbořil and P. Jelinek, On-surface structural and electronic properties of spontaneously formed Tb<sub>2</sub>Pc<sub>3</sub> single molecule magnets, *Nanoscale*, 2018, **10**, 15553.
- 10 F. Ciccullo, M. Glaser, M. S. Sättele, S. Lenz, P. Neugebauer, Y. Rechkemmer, J. van Slageren, M. B. Casu

- and M. B. Casu, Thin film properties and stability of a potential molecular quantum bit based on copper(II), *J. Mater. Chem. C*, 2018, **6**, 8028.
- 11 J. Hrubý, D. Dvořák, L. Squillantini, M. Mannini, J. van Slageren, R. Herchel, I. Nemec and P. Neugebauer, Co(II)-Based single-ion magnets with 1,1'-ferrocenediyl-bis(diphenylphosphine) metalloligands, *Dalton Trans.*, 2020, **49**, 11697.
  - 12 A. K. Mondal, T. Goswami, A. Misra and S. Konar, Probing the Effects of Ligand Field and Coordination Geometry on Magnetic Anisotropy of Pentacoordinate Cobalt(II) Single-Ion Magnets, *Inorg. Chem.*, 2017, **56**, 6870.
  - 13 T. Jurca, A. Farghal, P. H. Lin, I. Korobkov, M. Murugesu and D. S. J. Richeson, Single-Molecule Magnet Behavior with a Single Metal Center Enhanced through Peripheral Ligand Modifications, *J. Am. Chem. Soc.*, 2011, **133**, 15814.
  - 14 B. Brachňáková, S. Matejová, J. Moncol, R. Herchel, J. Pavlik, E. Moreno-Pineda, M. Ruben and I. Šalitroš, Stereochemistry of coordination polyhedra vs. single ion magnetism in penta- and hexacoordinated Co(II) complexes with tridentate rigid ligands, *Dalton Trans.*, 2020, **49**, 1249.
  - 15 N. Malinová, J. Juráková, B. Brachňáková, J. Dubnická-Midlíková, E. Čížmár, V. T. Santana, R. Herchel, M. Orlita, I. Mohelský, J. Moncol, P. Neugebauer and I. Šalitroš, Magnetization Slow Dynamics in Mononuclear Co(II) Field-Induced Single-Molecule Magnet, *Cryst. Growth Des.*, 2023, **23**, 2430.
  - 16 S. Q. Su, S. Q. Wu, M. L. Baker, P. Bencok, N. Azuma, Y. Miyazaki, M. Nakano, S. Kang, Y. Shiota, K. Yoshizawa, S. Kanegawa and O. Sato, Quenching and Restoration of Orbital Angular Momentum through a Dynamic Bond in a Cobalt(II) Complex, *J. Am. Chem. Soc.*, 2020, **142**, 11434.
  - 17 (a) S. Alvarez, D. Avnir, M. Llunell and M. Pinsky, Continuous symmetry maps and shape classification. The case of six-coordinated metal compounds, *New J. Chem.*, 2002, **26**, 996; (b) M. Llunell, D. Casanova, J. Cirera, P. Alemany and S. Alvarez, *SHAPE version 2.0*, Universitat de Barcelona, Barcelona, 2010.
  - 18 M. G. B. Drew, C. J. Harding, V. McKee, G. G. Morgan and J. Nelson, Geometric control of manganese redox state, *J. Chem. Soc., Chem. Commun.*, 1995, **10**, 1035.
  - 19 (a) R. D. Deegan, O. Bakajin, T. F. Dupont, G. V. Huber, S. R. Nagel and T. A. Witten, *Nature*, 1997, **389**, 827; (b) M. Cavallini, *J. Mater. Chem.*, 2009, **19**, 6085.
  - 20 (a) M. Cavallini, D. Gentili, P. Greco, F. Valle and F. Biscarini, Capillary flow as the cause of ring stains from dried liquid drops, *Nat. Protoc.*, 2012, **7**, 1668; (b) T. Mallah and M. Cavallini, Surfaces, thin films and patterning of spin crossover compounds, *C. R. Chim.*, 2018, **21**, 1270.
  - 21 D. Gentili, P. Sonar, F. Liscio, T. Cramer, L. Ferlauto, F. Leonardi, S. Milita, A. Dodabalapur and M. Cavallini, *Nano Lett.*, 2013, **13**, 3643.
  - 22 (a) I. Nemec, R. Herchel and Z. Trávníček, *Dalton Trans.*, 2016, **45**, 12479; (b) L. Havlíček, R. Herchel, I. Nemec and P. Neugebauer, Weak antiferromagnetic interaction in Cu (II) complex with semi-coordination exchange pathway, *Polyhedron*, 2022, **223**, 115962.
  - 23 (a) F. Neese, Software update: the ORCA program system, version 4.0, *Wiley Interdiscip. Rev.: Comput. Mol. Sci.*, 2018, **8**, e1327; (b) F. Neese, F. Wennmohs, U. Becker and C. Riplinger, *J. Chem. Phys.*, 2020, **152**, 224108.
  - 24 F. Weigend and R. Ahlrichs, The ORCA quantum chemistry program package, *Phys. Chem. Chem. Phys.*, 2005, **7**, 3297.
  - 25 R. F. W. Bader, Atoms in molecules, *Acc. Chem. Res.*, 1985, **18**, 9.
  - 26 (a) T. Lu and F. Chen, Multiwfn: A multifunctional wavefunction analyzer, *J. Comput. Chem.*, 2012, **33**, 580; (b) T. Lu and F. Chen, Quantitative analysis of molecular surface based on improved Marching Tetrahedra algorithm, *J. Mol. Graphics Modell.*, 2012, **38**, 314.
  - 27 E. R. Johnson, S. Keinan, P. Mori-Sánchez, J. Contreras-García, A. J. Cohen and W. Yang, Revealing Noncovalent Interactions, *J. Am. Chem. Soc.*, 2010, **132**, 6498.
  - 28 P.Å. Malmqvist and B. O. Roos, The CASSCF state interaction method, *Chem. Phys. Lett.*, 1989, **155**, 189.
  - 29 (a) C. Angeli, R. Cimiraglia and J. P. Malrieu, *Chem. Phys. Lett.*, 2001, **350**, 297; (b) C. Angeli, R. Cimiraglia, S. Evangelisti, T. Leininger and J. P. Malrieu, N-electron valence state perturbation theory: a fast implementation of the strongly contracted variant, *J. Chem. Phys.*, 2001, **114**, 10252.
  - 30 (a) F. Weigend, Accurate Coulomb-fitting basis sets for H to Rn, *Phys. Chem. Chem. Phys.*, 2006, **8**, 1057; (b) A. Hellweg, C. Hättig, S. Höfener and W. Klopper, Optimized accurate auxiliary basis sets for RI-MP2 and RI-CC2 calculations for the atoms Rb to Rn, *Theor. Chem. Acc.*, 2007, **117**, 587.
  - 31 (a) R. Izsák and F. Neese, An overlap fitted chain of spheres exchange method, *J. Chem. Phys.*, 2011, **135**, 144105; (b) F. Neese, F. Wennmohs, A. Hansen and U. Becker, Efficient, approximate and parallel Hartree-Fock and hybrid DFT calculations. A 'chain-of-spheres' algorithm for the Hartree-Fock exchange, *Chem. Phys.*, 2009, **356**, 98.
  - 32 (a) D. M. P. Mingos, P. Day and J. P. Dahl, *Molecular Electronic Structures of Transition Metal Complexes II*, Springer, Berlin/Heidelberg, 2012; (b) S. K. Singh, J. Eng, M. Atanasov and F. Neese, Covalency and chemical bonding in transition metal complexes: An ab initio based ligand field perspective, *Coord. Chem. Rev.*, 2017, **344**, 2.
  - 33 S. Gomez-Coca, E. Cremades, N. Aliaga-Alcalde and E. Ruiz, Mononuclear Single-Molecule Magnets: Tailoring the Magnetic Anisotropy of First-Row Transition-Metal Complexes, *J. Am. Chem. Soc.*, 2013, **135**(18), 7010.
  - 34 R. Boča, *A Handbook of Magnetochemical Formulae*, Elsevier, Amsterdam, 2012.
  - 35 R. Boča and R. Herchel, *POLYMAGNET*, 2006–2022.
  - 36 R. Herchel, L. Váhovská, I. Potočník and Z. Trávníček, Slow Magnetic Relaxation in Octahedral Cobalt(II) Field-Induced Single-Ion Magnet with Positive Axial and Large Rhombic Anisotropy, *Inorg. Chem.*, 2014, **53**, 5896.
  - 37 J. Telser, EPR Interactions – Zero Field Splittings, *eMagRes*, 2017, **6**, 207.
  - 38 (a) J. van Slageren, S. Vongtragool, B. Gorshunov, A. A. Mukhin, N. Karl, J. Krzystek, J. Telser, A. Müller, C. Sangregorio, D. Gatteschi and M. Dressel, Frequency-



- domain magnetic resonance spectroscopy of molecular magnetic materials, *Phys. Chem. Chem. Phys.*, 2003, **5**, 3837; (b) A. A. Pavlov, D. Y. Aleshin, S. A. Savkina, A. S. Belov, N. N. Efimov, J. Nehrkorn, M. Ozerov, Y. Z. Voloshin, Y. V. Nelyubina and V. V. Novikov, A Trigonal Prismatic Cobalt(II) Complex as a Single Molecule Magnet with a Reduced Contribution from Quantum Tunneling, *ChemPhysChem*, 2019, **20**, 1001; (c) J. Vallejo, M. Viciano-Chumillas, F. Lloret, M. Julve, I. Castro, J. Krzystek, M. Ozerov, D. Armentano, G. De Munno and J. Cano, Coligand Effects on the Field-Induced Double Slow Magnetic Relaxation in Six-Coordinate Cobalt(II) Single-Ion Magnets (SIMs) with Positive Magnetic Anisotropy, *Inorg. Chem.*, 2019, **58**, 15726; (d) E. Ya. Misochko, A. V. Akimov, D. V. Korchagin, J. Nehrkorn, M. Ozerov, A. V. Palii, J. M. Clemente-Juan and S. M. Aldoshin, Purely Spectroscopic Determination of the Spin Hamiltonian Parameters in High-Spin Six-Coordinated Cobalt(II) Complexes with Large Zero-Field Splitting, *Inorg. Chem.*, 2019, **58**(24), 16434; (e) A. Landart-Gereka, M. M. Quesada-Moreno, I. F. Díaz-Ortega, H. Nojiri, M. Ozerov, J. Krzystek, M. A. Palacios and E. Colacio, Large easy-axis magnetic anisotropy in a series of trigonal prismatic mononuclear cobalt(II) complexes with zero-field hidden single-molecule magnet behaviour: the important role of the distortion of the coordination sphere and intermolecular interactions in the slow relaxation, *Inorg. Chem. Front.*, 2022, **9**, 2810.
- 39 D. H. Moseley, S. E. Stavretis, K. Thirunavukkuarasu, M. Ozerov, Y. Cheng, L. L. Daemen, J. Ludwig, Z. Lu, D. Smirnov, C. M. Brown, A. Pandey, A. J. Ramirez-Cuesta, A. C. Lamb, M. Atanasov, E. Bill, F. Neese and Z.-L. Xue, Spin-phonon couplings in transition metal complexes with slow magnetic relaxation, *Nat. Commun.*, 2018, **9**, 2572.
- 40 (a) S. Stoll and A. Schweiger, EasySpin, a comprehensive software package for spectral simulation and analysis in EPR, *J. Magn. Reson.*, 2006, **178**, 42; (b) J. Nehrkorn, J. Telser, K. Holldak, S. Stoll and A. Schnegg, Simulating Frequency-Domain Electron Paramagnetic Resonance: Bridging the Gap between Experiment and Magnetic Parameters for High-Spin Transition-Metal Ion Complexes, *J. Phys. Chem. B*, 2015, **119**(43), 13816.
- 41 A. V. Palii, D. V. Korchagin, E. A. Yureva, A. V. Akimov, E. Y. Misochko, G. V. Shilov, A. D. Talantsev, R. B. Morgunov, S. M. Aldoshin and B. S. Tsukerblat, Single-Ion Magnet  $\text{Et}_4\text{N}[\text{Co}^{\text{II}}(\text{hfac})_3]$  with Nonuniaxial Anisotropy: Synthesis, Experimental Characterization, and Theoretical Modeling, *Inorg. Chem.*, 2016, **55**, 9696.
- 42 S. Gómez-Coca, A. Urtizberea, E. Cremades, P. J. Alonso, A. Camón, E. Ruiz and F. Luis, Origin of slow magnetic relaxation in Kramers ions with non-uniaxial anisotropy, *Nat. Commun.*, 2014, **5**, 4300.
- 43 (a) K. N. Shrivastava, Theory of Spin-Lattice Relaxation, *Phys. Status Solidi B*, 1983, **117**, 437; (b) A. Singh and K. Shrivastava, Optical-acoustic two-phonon relaxation in spin systems, *Phys. Status Solidi B*, 1979, **95**, 273.
- 44 R. L. Carlin, *Magnetochemistry*, Springer-Verlag, Berlin, 1986.